Soft Matter

PAPER

View Article Online
View Journal | View Issue

Cite this: *Soft Matter*, 2019, **15**, 3353

Image-based analysis of uniaxial ring test for mechanical characterization of soft materials and biological tissues

Eline E. van Haaften, [ab] Mark C. van Turnhout [a] and Nicholas A. Kurniawan †*[ab]

Received 16th November 2018,
Accepted 15th March 2019

DOI: 10.1039/c8sm02343c

rsc.li/soft-matter-journal

Uniaxial ring test is a widely used mechanical characterization method for a variety of materials, from industrial elastomers to biological materials. Here we show that the combination of local material compression, bending, and stretching during uniaxial ring test results in a geometry-dependent deformation profile that can introduce systematic errors in the extraction of mechanical parameters. We identify the stress and strain regimes under which stretching dominates and develop a simple image-based analysis approach that eliminates these systematic errors. We rigorously test this approach computationally and experimentally, and demonstrate that we can accurately estimate the sample mechanical properties for a wide range of ring geometries. As a proof of concept for its application, we use the approach to analyze explanted rat vascular tissues and find a clear temporal change in the mechanical properties of these explants after graft implantation. The image-based approach can therefore offer a straightforward, versatile, and accurate method for mechanically characterizing new classes of soft and biological materials.

1 Introduction

Mechanical characterization of ring-shaped materials traditionally employ uniaxial ring test, where the specimen is mounted between two arms and subjected to extension through a prescribed movement of the arms. The distance between the arms and the force required to apply the arm movement are recorded and used to calculate the material properties. The simplicity of the method makes it attractive for the characterization of a wide range of materials, ranging from ring-shaped hydrogels[1] to food products.[2] Indeed, the uniaxial ring test is the official standard for tensile testing of elastomers (ASTM D 1414),[3] established for use by the O-ring industry.[4]

More recently, uniaxial ring test has also found a large application area in the mechanical characterization of biological tissues and biomaterials. In particular, uniaxial ring test has been increasingly shown to be the method of choice for the assessment of mechanical properties of blood vessels and blood vessel substitutes, due to its ability to mimic the physiological loading in the circumferential direction.[5–7] Moreover, uniaxial ring test allows mechanical characterization of small and delicate vascular specimens, for which other testing methods such as uniaxial tensile test of cut-out sample strips and biaxial test of planar samples are unfeasible or can introduce undesired measurement artifacts.[8–11] As such, biomedical researchers have started to explore the usefulness of uniaxial ring test for the mechanical measurement of small blood vessels,[12] vascular grafts,[12,13] tissue-engineered vascular constructs,[14,15] and even arterial tissues.[7] Such mechanical assessments are important not only for improving the design of vascular constructs and developing mathematical models,[16,17] but also for understanding and diagnosing various vascular diseases.[18,19]

One key challenge that commonly arises in the uniaxial ring test is the extraction of useful material parameters from the raw measurement data. A typical approach is by fitting the force *vs.* arm distance (or pin displacement) data to a linear function, from which the Young's modulus of the material is inferred. However, in a uniaxial ring test, the initial force response recorded on the pins contains a mixed contribution from bending and stretching forces, as the ring is deformed to a straight shape. Furthermore, as we shall show in this article, during this initial bending stage, pin displacements are not a suitable measurement metric for material stretches. These effects make accurate and reliable material parameters estimation from force–displacement curves a challenge.

[a] *Department of Biomedical Engineering, Eindhoven University of Technology, The Netherlands*
[b] *Institute for Complex Molecular Systems, Eindhoven University of Technology, The Netherlands*
† Department of Biomedical Engineering, Eindhoven University of Technology, P.O. Box 513, 5600 MB Eindhoven, The Netherlands. E-mail: kurniawan@tue.nl

We propose that there exists a stretch regime under which the bending and stretching contributions can be sufficiently separated, so that the material properties can be accurately estimated from a uniaxial ring test without using inverse analysis. This knowledge will greatly expand the use of the uniaxial ring test method for the characterizations of new classes of materials, especially when the material behavior is not *a priori* known, for example in the context of soft hydrogels and biological materials.

In this work, we demonstrate that deformation above a certain critical stretch in uniaxial ring tests is effectively dominated by stretching, thereby allowing accurate estimation of material mechanical stiffness. We further propose a simple image-based approach that both exploits this idea and circumvents the current problem with stretch estimation from pin displacement. We validate our approach computationally and experimentally through a direct comparison with uniaxial tensile testing measurements, and quantify how various parameters such as ring geometry can affect the analysis and outcomes. Finally, we show a proof of concept where we apply the method to characterize the temporal change in the mechanical properties as a result of tissue formation and scaffold degradation in explants from aortic interposition grafts in rats.

2 Materials and methods

In a uniaxial ring test, a ring-shaped specimen is stretched by two pins that move in opposite directions. We first assess the merit of our approach numerically and investigate how experimental parameters affect the extraction of the sample stiffness E_{ring}. We then propose an image-based tracking algorithm to estimate sample stretch in uniaxial ring experiments and we compare our estimate of E_{ring} against the Young's modulus that we measured in uniaxial tensile tests on the same material.

2.1 Computational method

2.1.1 Finite element model. The samples are modeled as rings with an initial inner radius R, thickness t, and height h, whereas the pin is modeled as a cylindrical rigid surface with a radius r (Fig. 1A). Frictionless contact is prescribed between the pin and the inside of the ring, and the ring is stretched in 100 increments by displacement of the ring in the positive x-direction for a total displacement of R. Thanks to symmetry, only one eighth of the ring is necessary to be simulated: half the height of a quadrant of the complete ring (Fig. 1A). Symmetrical boundary conditions are prescribed for the ring for the cross section in the yz-plane, the cross section in the xz-plane (at the pin), and the xy-plane at the bottom of the mesh (*i.e.*, symmetry over the height).

All finite element (FE) simulations were performed with Simulia Abaqus 6.14-1 (Dassault Systèmes Simulia Corp., Providence, RI, USA). The ring is meshed with 20-node quadratic brick elements (C3D20RH) that are kept approximately equal in size (determined with initial mesh convergence tests) for all simulations. We use an isotropic compressible Neo-Hookean material model for the ring with strain energy potential function:

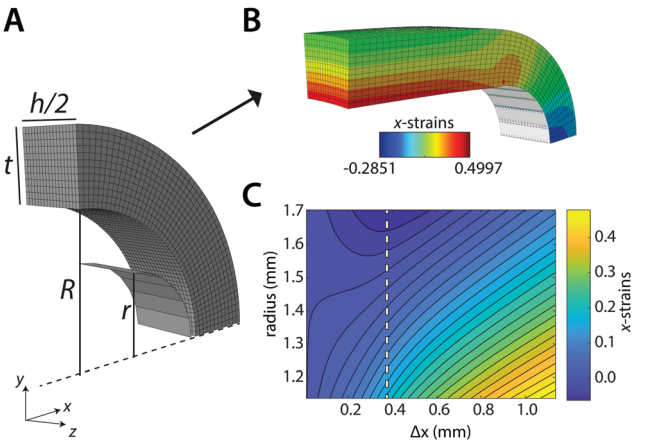

Fig. 1 Computational model. Geometry of the ring (A) before and (B) after the simulated uniaxial ring test. (C) Contour plot of the strains in the x-direction as a function of the radial distance in the ring (*i.e.*, across the ring thickness t) and pin displacement Δx. The *dashed line* indicates the point of maximum compression.

$$U = \frac{\mu_0}{2}(\bar{\lambda}_1^2 + \bar{\lambda}_2^2 + \bar{\lambda}_3^2 - 3) + \frac{\kappa_0}{2}(J-1)^2 \quad (1)$$

with μ_0 the shear modulus, $\bar{\lambda}_i = J^{-\frac{1}{3}}\lambda_i$ the deviatoric principal stretches, J the determinant of the deformation gradient tensor $\mathbf{F}$, and κ_0 the compression modulus. The shear modulus μ_0 and compression modulus κ_0 are derived from the Young's modulus E and Poisson's ratio ν as:

$$\mu_0 = \frac{E}{2(1-\nu)} \quad (2)$$

$$\kappa_0 = \frac{\mu_0(1+\nu)}{3(1-2\nu)} \quad (3)$$

The following read-outs are recorded: the reaction force in x-direction on the pin, the initial coordinates and displacements of the nodes on the outer perimeter of the ring in the xy-symmetry plane (*i.e.*, bottom of the mesh) and of the highest node in the yz-symmetry plane of the ring, and the strains in x-direction for the nodes in the yz-symmetry plane of the ring. These read-outs are post-processed with Matlab (R2015a, the Mathworks, Matick, MA, USA).

We calculate the stress σ_{ring} for the ring in each displacement increment using $\sigma_{\text{ring}} = F/A$, where F is the reaction force on the pin. A is the cross-sectional area of the ring in the yz-symmetry plane, as obtained from the coordinates and displacements of the highest node on the outer perimeter and those of the opposite node in the inner perimeter of the ring.

Because of sample bending during the uniaxial ring test, pin displacement is not suitable for the assessment of ring stretches. Instead, we use the stretch of the outer perimeter of the ring λ_{OP}, calculated for each increment in the simulation, as a measurement metric of ring stretch. We further propose that at sufficiently large pin displacements, sample deformation is dominated by stretching. Therefore, we anticipate that: (1) λ_{OP}

becomes linear in pin displacements; and (2) stresses in the ring become linear in λ_{OP} (in the symmetry plane between the pins). Following these premises, we estimate the Young's modulus of the ring that is being tested, E_{ring}, as:

$$E_{ring} = \frac{\Delta\sigma_{ring}}{\Delta\lambda_{OP}} \quad (4)$$

In practice, the initial bending also results in compressive strains in the *yz*-symmetry plane of the ring. We use the strains in *x*-direction over this plane to find the point of maximum compression: $\lambda_{\pm}$. For $\lambda_{OP} > \lambda_{\pm}$, all the strains over this cross section monotonically increase in the simulations (Fig. 1C, dashed line). We then estimate E_{ring} with $\Delta\lambda_{OP} = 2.5\%$, starting at $\lambda_{\pm} + 2.5\%$:

$$E_{ring} = \frac{\sigma_{ring}(\lambda_{\pm} + 5\%) - \sigma_{ring}(\lambda_{\pm} + 2.5\%)}{2.5\%} \quad (5)$$

2.1.2 Sensitivity analysis. Experimental parameters, such as the ring geometry, Poisson's ratio, as well as the pin radius, can affect the bending modes and therefore the accuracy of the extraction of material parameters in a uniaxial ring test. To investigate this effect, we performed a sensitivity analysis by running 100 simulations of ring deformations. For each simulation, we pulled random variables from a uniform distribution of the parameter space, with the geometry of the ring and the pin, and the mechanical properties of the ring as experimental variables (Table 1). Specifically, we explored the effects of the inner radius of the ring R, the height of the ring h, the thickness of the ring t, the pin radius r, the ring's stiffness E and the ring's Poisson's ratio ν. From these 100 simulations, we calculate $\lambda_{\pm}$ and E_{ring} (eqn (5)).

We investigate the effects of the explored parameters on $\lambda_{\pm}$ and E_{ring} with a multiple linear regression model. Buckingham π theorem was used to define a nondimensional equation by constructing the following dimensionless groups out of the dimensioned variables:

$$\pi_1 = \frac{E}{E_{ring}}; \quad \pi_2 = \frac{t}{R}; \quad \pi_3 = \frac{h}{R}; \quad \pi_4 = \frac{r}{R}, \quad (6)$$

giving us the following regression model:

$$y = a_1 + a_2\pi_2 + a_3\pi_3 + a_4\pi_4 + a_5\nu + \text{error} \quad (7)$$

with $y = \lambda_{\pm}$ or $y = \pi_1$. We report the coefficients, their 95% confidence intervals, the fraction of the variation that is explained by the parameter (the associated sum of squares divided by the total sum of squares), and the associated *p*-values.

Table 1 Overview of tested parameter space in the sensitivity analysis

Symbol	Property	Unit	Parameter space
R	Inner ring radius	mm	[0.5–2.5]
h/R	Ring height to radius	—	[0.2–4.0]
t/R	Ring thickness to radius	—	[0–1]
r/R	Pin radius to radius	—	[0.1–0.9]
E	Young's modulus	MPa	[0.1–5.1]
ν	Poisson's ratio	—	[0–0.475]

Table 2 Geometrical properties of the rings in the experimental validation (mean ± std, n = 3)

Group	h (mm)	R (mm)	t (mm)	t/R (−)
1	0.69 ± 0.00	0.92 ± 0.01	0.48 ± 0.02	0.52 ± 0.02
2	0.68 ± 0.00	0.97 ± 0.01	0.29 ± 0.03	0.30 ± 0.03
3	0.67 ± 0.01	1.43 ± 0.01	0.27 ± 0.03	0.19 ± 0.02

2.2 Experimental method

2.2.1 Mechanical tests. Uniaxial ring tests were performed in a modified biaxial tensile tester setup (CellScale Biomaterial Testing, Waterloo, Canada), equipped with a 5000 mN load cell. To test for the validity of the proposed approach, ring shaped samples with various geometries were punched from a rubber flap (thickness ≈ 700 μm) and subjected to the tensile test. Prior to mounting, the height h, radius R, and thickness t of the rings were measured at multiple locations with a digital microscope (Keyence VHX-500FE, Table 2). The rings were mounted onto the tensile tester using two stainless steel pins (∅ ≈250 μm) that were fixed in the testing device with magnets (Fig. 4A). The rings were deformed at 10 mm min^{-1} crosshead speed until failure, and the associated forces and displacements were recorded at a frequency of 5 Hz. The stretch λ_{OP} was defined as the outer perimeter length normalized to initial outer perimeter length, calculated *via* image analysis (see Section 2.2.2). Assuming isotropic material properties, the estimated ring stress was derived from the force and displacement measurements:

$$\sigma_{ring} = \frac{F}{A} = \frac{F}{\lambda_{tr}^2 A_0} \quad (8)$$

with the transverse stretch, λ_{tr}, calculated *via*:

$$\lambda_{tr} = 1 - \nu(\lambda_{OP} - 1) \quad (9)$$

The Poisson's ratio was calculated from the uniaxial tensile testing data, and set at ν = 0.41. With σ_{ring} and λ_{OP}, we use eqn (5) to estimate E_{ring}.

To compare the uniaxial ring test results against traditional uniaxial tensile data, dogbone shaped samples (n = 4) from the same material were uniaxially stretched in the biaxial tensile tester at the same crosshead speed of 10 mm min^{-1}. Before mounting the sample, graphite particles were applied onto the surface facilitating optical strain analysis by digital image correlation (using LabJoy software, Fig. 4B). Assuming isotropic material properties, the Poisson's ratio was derived from the slopes of the longitudinal and transverse stretch, up to a longitudinal stretch of 1.2 (eqn (9)). Similar to the ring tests, we calculate the ratio between σ and λ over a 2.5% stretch range, starting at λ = 2.5%:

$$E = \frac{\sigma(\lambda = 5\%) - \sigma(\lambda = 2.5\%)}{2.5\%} \quad (10)$$

2.2.2 Displacement tracking. To obtain the ring stretch in a robust manner, we developed an image-based tracking algorithm that computes the outer perimeter length of the ring (in pixels), allowing the user to calculate the outer perimeter stretch λ_{OP}. To minimize analysis artifacts arising from sample

and image irregularities, the outer perimeter length is obtained based on the circumference of a super ellipse that is fitted through a set of 20 points on this outer perimeter.

In short, the image is converted into a binary image with sample coordinates (X, Y). For the image of the undeformed samples, this set of coordinates is fitted with an ellipse to calculate the center of mass (*i.e.* x_0, y_0), the major and minor axes a and b, and the orientation ϕ. However, at larger stretches, an ellipse cannot accurately describe the outline of the sample. Therefore, a shape parameter n is introduced, which transforms the ellipse into a super ellipse. We use the fit of the ordinary ellipse as an initial guess for this super ellipse. The parameters x_0, y_0 and ϕ are fixed, and with those we fit the parametric form of the super ellipse:

$$\left.\begin{aligned} x(t) &= |\cos t|^{2/n} \cdot a \cdot \mathrm{sgn}(\cos t) \\ y(t) &= |\sin t|^{2/n} \cdot b \cdot \mathrm{sgn}(\cos t) \end{aligned}\right\} 0 \le t < 2\pi \qquad (11)$$

where a and b denote the major and minor axes. For $n = 2$, the curve reduces to an ordinary ellipse.

We select a number of points on the outer perimeter of (X,Y) and compare their distance to the center of mass with the distance of the estimated super ellipse to the center of mass. With the fminsearch function in Matlab, we minimize the root-mean-square (RMS) of the differences in distances between the sample points and the corresponding super ellipse points. Using this approach, any number of data points can be generated and used to calculate the RMS. Here, t is discretized into 20 points between 0 and 2π, resulting in excellent shape-fitting results (Fig. 2B).

This algorithm, schematically depicted in Fig. 2A, is implemented in Matlab and is made freely accessible *via* https://gitlab.tue.nl/stem/orlab.

2.3 Measurements of *ex vivo* biological samples

As a proof of concept, explants from aortic interposition grafts in rats were subjected to the uniaxial ring test to characterize the temporal change in mechanical properties as a result of *de novo* tissue formation and scaffold degradation. Briefly, the vascular scaffolds (2 mm inner diameter, 280 μm thickness, 5 μm fibers) were prepared from supramolecular polycaprolactone-based elastomeric polymers[20] using electrospinning. The extremities were shielded by an impenetrable Gore-Tex strip to prevent anastomotic ingrowth. The Gore-Tex shielded scaffolds were then implanted as abdominal aorta interposition grafts in rats for up to 3 months. All animal experiments were reviewed and approved by the Institutional Animal Care and Use Committee of the University of Utrecht, The Netherlands, and conform to the guidelines for the use of laboratory animals as formulated by the Dutch Law on animal experimentation. For a detailed description of the *in vivo* study, the reader is referred to Bonito[21] At selected time points, ring-shaped explants were harvested, snap-frozen in liquid nitrogen, and stored at −80 °C until analysis. All mechanical tests were performed in a phosphate-buffered saline bath at 37 °C and analyzed according to the method presented in Section 2.2.

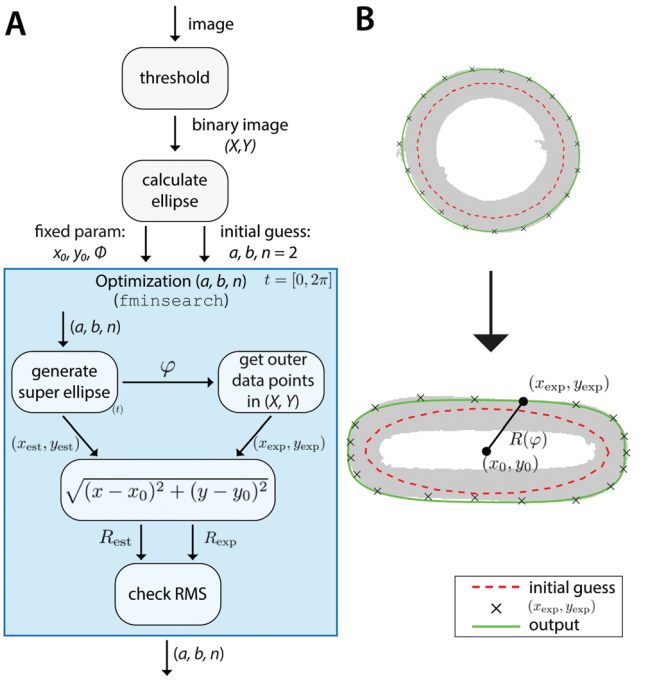

Fig. 2 Image-based estimation of λ_{OP}. (A) Schematic of displacement tracking algorithm. (B) Example of optimization result with the initial ellipse fit (dashed red), and the final super ellipse fit to the perimeter (green) for an undeformed (top) and deformed (bottom) sample. The sample contours are shown in gray.

3 Results

3.1 Simulations of uniaxial ring test

We first tested our assumption that for large pins displacements λ_{OP} indeed becomes linear with pin displacements Δx (Fig. 3A); and that the estimate of ring tensile stress σ_{ring} from pin reaction forces and ring cross sectional area becomes linear with λ_{OP} (Fig. 3B, blue). This validates our use of λ_{OP} and σ_{ring} in the analysis. Note that the pin reaction force itself (uncorrected for area changes) does not necessarily become linear in λ_{OP} (Fig. 3B, red). The strain contour plots show that, due to bending of the ring shape during uniaxial ring test, the material undergoes local compression and tension (Fig. 1B and C). However, at large pin displacements, tensile strains become linear over the entire cross section of the ring.

We next asked whether the point of maximum compression is influenced by the geometry of the ring samples and the pin, as well as the Poisson's ratio of the sample. To rigorously test this, we run a large number of simulations with varying experimental parameters and statistically analyzed the results using a multiple linear regression model to find the key parameters that sensitively affect the deformation mode. For the point of maximum compression in the simulations we find:

$$\lambda_{\pm} = 1.005 + 0.048\frac{t}{R} + 0.000\frac{h}{R} - 0.011\frac{r}{R} + 0.013\nu + \mathrm{error} \qquad (12)$$

Ring height h does not affect $\lambda_{\pm}$, as demonstrated by the near-zero coefficient and the associated variation and the large

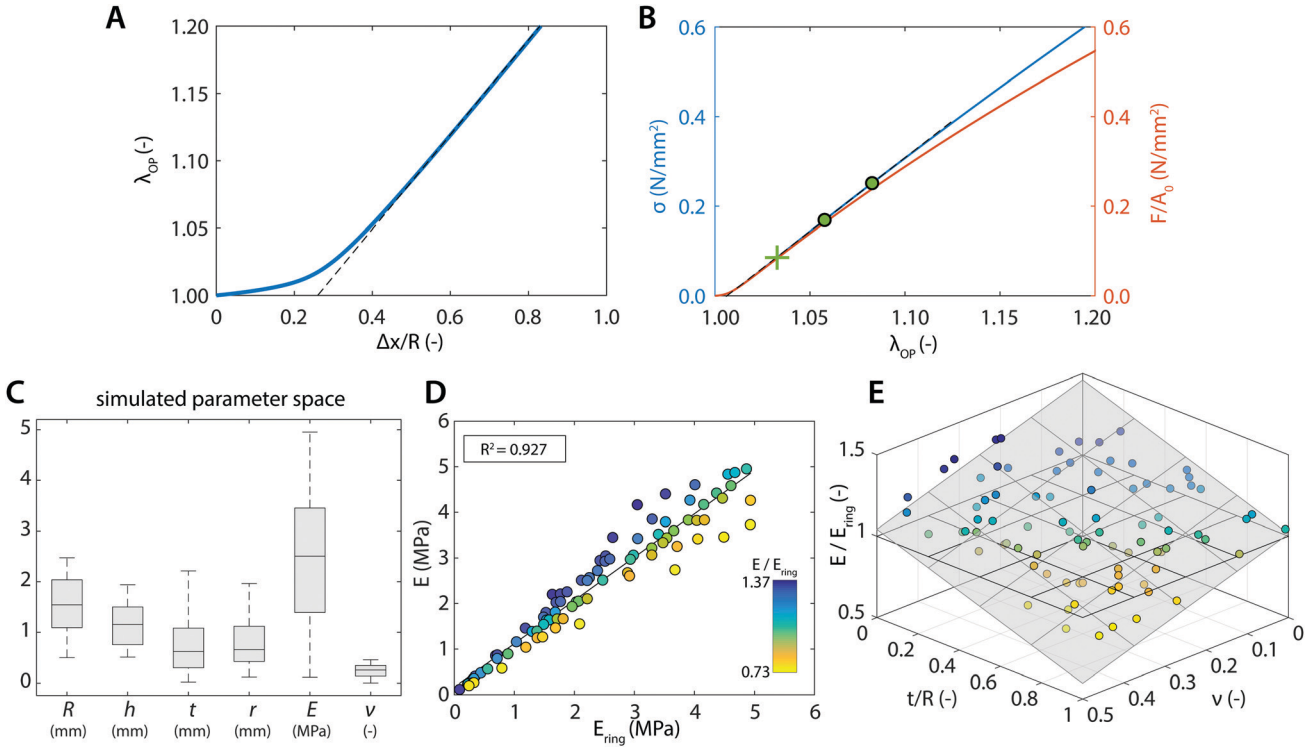

Fig. 3 Simulation results. (A) Relation between the outer perimeter stretch λ_{OP} and the pin displacement Δx (normalized to ring radius R). The linear region is indicated by the dashed line. (B) The resulting stress–stretch relation based on the true area (blue axis) or the initial area A_0 (red axis). The green cross indicates the location of $\lambda_{\pm}$, and the green dots indicate the region used to estimate E. (C) The tested random variables in the sensitivity analysis for extracting E_{ring}. (D) Correlation between the true stiffness, E, and stiffness obtained from the uniaxial ring simulations, E_{ring}. (E) Ratio of the true stiffness and calculated stiffness by uniaxial ring simulations as a function of t/R and ν (gray plane represents a linear fit through the data points, horizontal plane indicates the case of a one-to-one correspondence).

p-value (Table 3). The normalized pin radius r/R (coefficient − 0.011, p = 0.001) and the Poisson's ratio ν (coefficient 0.013, p = 0.027) together contribute <4% to the variation in the model. The largest coefficient (0.048) is positively associated with normalized thickness t/R, and explains 75% of the variation in the model ($p < 0.001$). About 21% of the variation in the model is unaccounted for by these variables.

These results suggest that for $r/R \ll 1$ the variation in $\lambda_{\pm}$ can be largely attributed to variation in the thickness of the ring t/R. When we apply a *post hoc* linear regression analysis, we find that:

$$\lambda_{\pm} = 1.005 + 0.046\frac{t}{R} \quad (13)$$

with an adjusted R^2 value of 0.736 (n = 100, $p < 0.001$) and 95% confidence interval for the intercept of [1.002 1.008] ($p < 0.001$) and for the slope of [0.040 0.051] ($p < 0.001$).

Not all simulations converged up to stretches of $\lambda_{\pm}$ + 5%, which is necessary for our analysis of E_{ring} (eqn (5)). Therefore we could only use 85 out of the 100 simulations that we ran, but this did not introduce a noteworthy bias in the uniform distribution of the tested parameter space (Fig. 3C). From these 85 simulations, we find for the relationship between the actual Young's modulus E and the estimated Young's modulus E_{ring}:

$$E = 0.950E_{ring} + 0.169 \quad (14)$$

with an adjusted R^2 value of 0.927 (n = 85, $p < 0.001$) and a 95% confidence interval for the slope of [0.892 1.007] ($p < 0.001$) and for the intercept of [0.012 0.326] (p = 0.035). The large correlation coefficient quantitatively validates the accuracy of our approach to estimate the actual ring stiffness E (Fig. 3D).

As can be seen from eqn (14), E_{ring} overestimates the actual E by 5% on average. For the remaining, small variation on this

Table 3 Multiple linear regression result for $\lambda_{\pm}$. From top to bottom: coefficients, coefficient 95% confidence intervals (CIs), fraction of variation explained by the parameter (sum of squares/total sum of squares), and the coefficients p-value

$\lambda_{\pm}$ =	1.005	+0.048t/R	+0.000h/R	−0.011r/R	+0.013ν	+ error
95% CI	0.999 1.011	0.043 0.053	−0.002 0.003	−0.017 −0.005	0.002 0.025	
SS/SS_{tot}		0.751	0.002	0.026	0.011	0.212
p	0.000	0.000	0.769	0.001	0.027	
n = 100						R_a^2 = 0.773

Table 4 Multiple linear regression result for E_{ring}. From top to bottom: coefficients, coefficient 95% confidence intervals (CIs), fraction of variation explained by the parameter (sum of squares/total sum of squares), and the coefficients p-value

E/E_{ring} =	1.387	$-0.445t/R$	$+0.020h/R$	$+0.042r/R$	-0.706ν	+ error
95% CI	1.338 1.437	−0.492 −0.340	0.001 0.040	−0.019 0.103	−0.807 −0.604	
SS/SS_{tot}		0.557	0.007	0.003	0.306	0.128
p	0.000	0.000	0.038	0.170	0.000	
n = 85						R_a^2 = 0.856

overestimation, we find (Table 4):

$$\frac{E}{E_{ring}} = 1.387 - 0.445\frac{t}{R} + 0.020\frac{h}{R} + 0.042\frac{r}{R} - 0.706\nu + \text{error} \quad (15)$$

Normalized ring height (coefficient 0.020, p = 0.038) and pin radius (coefficient 0.042, p = 0.171) together contribute only 1% to the total variation in the model. Normalized ring thickness t/R and Poisson's ratio ν each have a coefficient in the order of 0.1 ($p < 0.000$), and together they explain 85% of the variation in the model. About 12% of the variation in the model is unaccounted for by these variables.

These results indicate that the remaining variation can be best explained by t/R and ν: for larger t/R and ν, E_{ring} tends to become larger with respect to the actual E (Fig. 3E).

3.2 Experimental validation

Having established a method to accurately estimate material stiffness and eliminate systematic errors due to measurement geometry and sample mechanical properties, we now test this method experimentally. Using our tracking algorithm, an estimation of the outer perimeter stretch could be obtained with a root-mean-square below 1.5% of the estimated perimeter throughout the entire analysis (Fig. 4A). The stretch-time relation in Fig. 4A further confirms that the relation between λ_{OP} and pin displacement is initially nonlinear, but eventually becomes linear for large deformations. To compute the stresses, we normalize the recorded forces to true area (eqn (8) and (9)) with the Poisson's ratio that we measured in the uniaxial tensile tests (Fig. 4B, ν = 0.41). Since our simulation results show that sample geometry, particularly t/R affects sample deformation and therefore the estimation of the material mechanical

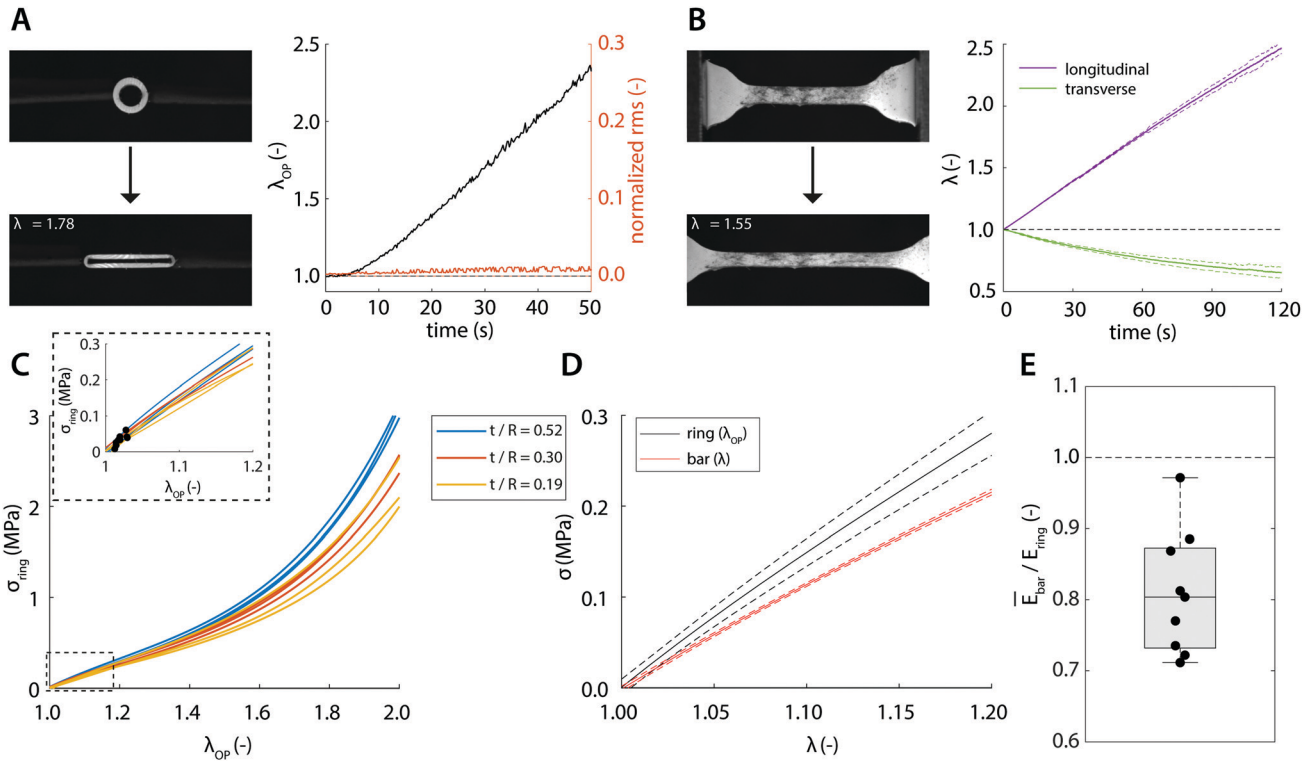

Fig. 4 Experimental results. Example image of (A) ring-shaped sample and (B) dog-bone-shaped sample prior to (top) and during stretching (bottom, the extent of stretch is indicated in the legend) with the associated displacement curves over time (right panels). (C) The resulting stress–stretch curves of ring-shaped samples with the different geometries indicated by the different colors. The inset shows zoom-in views for stretches up to 1.2; the black dots indicate $\lambda_{\pm}$ for each sample. (D) Comparison of the stress–stretch curves between ring-shaped samples (black) and dog-bone-shaped samples (red) (standard deviations indicated by dashed line). (E) Ratio of the calculated mean stiffness measured by tensile tests and the calculated stiffness measured by ring tests (box plot contains 50% of the data, central mark = median, dashed line indicates the case of a one-to-one correspondence).

properties, we tested rubber samples with varying sample geometries in the uniaxial ring test. The resulting experimental stress–stretch curves of the ring-shaped samples indeed corroborate the computational findings: for smaller t/R, the computed stresses tend to become smaller (Fig. 4C).

To directly compare the uniaxial ring test results against the 'conventional' uniaxial tensile test of the same material, we plot the average stress–stretch relations measured using the two techniques (Fig. 4D). It can be qualitatively observed that the curves are close to each other and that the computed stresses measured in the ring tests are slightly but consistently larger compared to those in the tensile tests. To make a quantitative comparison, we take into account the point of maximum compression $\lambda_{\pm}$, which is estimated *via* eqn (13) and highlighted in the inset of Fig. 4C. Using eqn (4), E_{ring} is estimated and compared against the average stiffness of the tensile test (Fig. 4E). We find that the stiffness estimated from the ring test (1.46 ± 0.15 MPa) agrees closely with the actual stiffness (1.17 ± 0.02 MPa), with only a minor discrepancy as predicted by our simulation results.

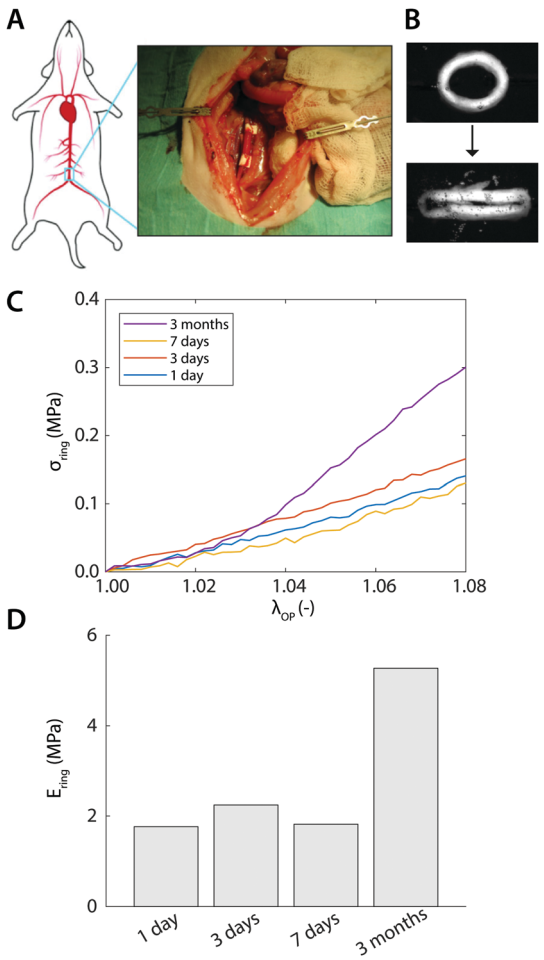

Fig. 5 *Ex vivo* results. (A) Surgical procedure of the scaffold implantation (image courtesy of Dr Valentina Bonito). (B) Explant at 3 months subjected to the uniaxial ring test. (C) Representative stress–stretch curves obtained after 1 day, 3 days, 7 days, and 3 months of implantation. (D) Temporal variations in E_{ring} during implantation time.

3.3 Uniaxial ring test of aortic grafts

With the established experimental method, we tested the mechanical properties of abdominal aorta interposition grafts that were implanted in rats for up to 3 months (Fig. 5A and B). At each explantation time point, the grafts exhibited a typical t/R ratio of around 0.2. The results show a clear temporal change in the mechanical behavior, especially between the early time points (up to 7 days) and the late time point (3 months, Fig. 5C). This change in mechanical behavior is consistent with the idea that initially the graft response is dominated by the properties of the scaffold, which is gradually degraded and replaced by the newly formed, stiffer vascular tissue. The extracted E_{ring} increases by a factor of >2 over the tested period, reflecting this stiffening trend (Fig. 5D).

4 Discussion

Uniaxial ring testing is a common method to identify material properties, including Young's modulus, yield stress and strain, and ultimate tensile stress and strain.[6,22–24] Furthermore, in the context of biomedical materials, clinically-important parameters such as burst pressure and compliance are also typically estimated from ring test data, through the application of Laplace's law, to characterize the functionality of (tissue engineered) vascular grafts.[25–27] In many of these applications, however, the pin-to-pin distance is used as the deformation metric for estimating the sample mechanical properties. As we show here, this approach, though simple, is inherently problematic as the deformation of the ring-shaped sample involves a combination of local compression, bending, and stretching. As a result, derivations of stretch are often highly susceptible to systematic errors. Moreover, the deformation profile and the relative contributions of stretching and bending are strongly affected by the sample and pin geometry and therefore difficult to identify, making the experimental force–strain relations hard to interpret.

In the present study, we offer a straightforward and accurate approach to estimate material stiffness from uniaxial ring test measurements. The simplicity of the approach is based on the notion that the contributions of sample bending and stretching in the force response can be well delineated from geometry alone, and thereby the outer perimeter stretch of the ring, λ_{OP}, can be used as a valid deformation metric (*i.e.*, instead of using the pin-to-pin distance). We develop a robust and freely-accessible algorithm for quantifying λ_{OP} from the measurement images and rigorously validate the approach computationally and experimentally.

The numerical simulations confirmed (1) that for large deformations, outer perimeter stretch λ_{OP} becomes linear with pin displacement; and (2) that for large deformations, the estimated ring stress from pin reaction forces and cross sectional area σ_{ring} becomes linear in λ_{OP} (Fig. 1B and 3A, B). Similarly, this linear behavior for large deformations was also confirmed in our experiments (Fig. 4A). The numerical simulations further showed that quantification of E_{ring} based on λ_{OP} is in very good agreement

with the actual stiffness E (eqn (4)). Extensive survey over a large parameter space shows that the actual stiffness is typically 5% lower than estimated by E_{ring} (eqn (14)), with outliers of up to $\approx$30% (Fig. 3E).

In the calculation of E_{ring}, we take into account that in the initial phase of the ring test the deformation is dominated by bending. With regard to this, our simulations revealed a simple empirical relation between the point of maximum compression (*i.e.*, monotonic extension over the entire cross section of the ring) and ring geometry (*i.e.*, t/R), independent of the intrinsic material properties (eqn (13)). Although ν (as a measure of incompressibility) and r/R (which affects the extent of ring bending) also contribute to this relation, their effects are negligible compared to t/R ($<$2.5% *vs.* 75%, Table 3), particularly when we consider that these effects are also limited by the possible range of the parameters: in general $0 < \nu < 0.5$, and by definition $0 < r/R < 1$. Using this relation, the stretch-dominating region in the ring test data can be identified and used to calculate a valid first-order, linear stiffness of the material (*i.e.*, E) without time-consuming and complex inverse analysis methods.

We emphasize that our proposed image-based analysis is optimally suited for the accurate extraction of this linear stiffness, which is particularly valuable in the field of vascular tissue engineering and biology. Extension of the approach to estimate other, non-linear parameters of soft tissues (for instance by a Fung material model) is possible, but inevitably requires an inverse analysis of some kind, because these parameters cannot be directly calculated from the slope of the σ–$\lambda_{\pm}$-curve.

The results from the simulations thus allow us to proceed with the experimental validation, where we tested ring-shaped and dog-bone-shaped samples from the same material. Taking into account the point of maximum compression for the calculation of E_{ring}, we found that the actual stiffness, as determined from the uniaxial tensile test, is typically 20% lower than E_{ring}, as determined from ring test data (Fig. 4E). This overestimation of E is larger than the 5% overestimation found by the simulations (eqn (14)) and can likely be attributed to experimental noise, which is common to all mechanical tests (*e.g.*, noise on force and displacement transducers, pixel discretization of the images, sample irregularities). In fact, due to the geometry and symmetry of uniaxial ring tests, the signal-to-noise ratio of ring tests is expected to be higher than that of conventional tensile tests.

It can be observed that previous studies that use the ring test approach to estimate burst pressures have also consistently shown to overestimate the actual burst pressure by between 25% and $>$400%.[25] Although these values cannot be directly compared to our results, it supports the idea that the ring-test method has a tendency to overestimate material properties. In fact, our simulations and experiments reveal that the degree of overestimation by E_{ring} is related to the geometry of the ring, t/R, and to the compressibility of the ring, ν (Fig. 3E and 4C): the larger these ratios, the larger the tendency to overestimate the stiffness. However, since Poisson's ratios of biological tissues typically fall in the narrow range of $0.3 < \nu < 0.5$, t/R remains the most relevant variable to account for. Based on this, we conclude that the accuracy of the method becomes better for relatively thin-walled ring samples, and that for a given t/R, the method is very sensitive to detect differences in stiffness. Therefore, it is recommended to always take into account this geometrical effect when comparing data from rings with different geometrical properties.

Finally, we applied the method, as an exemplary proof of concept, to measure the mechanical properties of ring-shaped vascular explants from rat aortic grafts. Given the agreement between the experimental and computational analysis, it is expected that the actual stiffness of the explants is slightly lower than the values reported in Fig. 5. Despite this, the temporal changes in mechanical properties, as a result of tissue formation and scaffold degradation, remain evident, illustrating the merit of this approach.

5 Conclusions

In conclusion, we have shown how the uniaxial ring test can be used to mechanically characterize soft materials and biological tissues, without the need for time consuming and complex inverse analysis methods. We offer a simple image-based analysis approach to determine the deformations in the tissue and provide an empirical relation to identify the stretch-dominating region of the force curve. This makes the uniaxial ring test a very attractive research tool for various research lines involving characterization of ring-shaped materials, even when the material behavior is not *a priori* known, including in the field of vascular tissue engineering and biology.

Conflicts of interest

The authors declare no conflicts of interest.

Acknowledgements

The authors would like to thank Dr Sandra Loerakker for her comments on the Finite Element modeling, as well as Dr Valentina Bonito and Dr Anthal Smits for sharing the raw data of the mechanical tests on the explants. We acknowledge support from the Netherlands's Ministry of Education, Culture, and Science (Gravitation program "Materials-Driven Regeneration").

References

1 J. H. Wu, P. F. Li, C. L. Dong, H. T. Jiang, B. Xue, X. Gao, M. Qin, W. Wang, B. Chen and Y. Cao, *Nat. Commun.*, 2018, **9**, 620.
2 H. Jung and W. B. Yoon, *J. Food Sci.*, 2017, **82**, 2894–2900.
3 A. International, *Annual Book of ASTM Standards; Section 9: RUBBER*, ASTM International, Conshohocken, USA, 2008, vol. 09.02 Rubber Products, Industrial Specifications and Related Test Methods; Gaskets; Tires.

4 J. R. Davis, *Tensile Testing*, ASM International, Materials Park, OH, 2nd edn, 2004.
5 M. J. Mulvany and W. Halpern, *Nature*, 1976, **260**, 617–619.
6 D. Seliktar, R. A. Black, R. P. Vito and R. M. Nerem, *Ann. Biomed. Eng.*, 2000, **28**, 351–362.
7 R. A. Macrae, K. Miller and B. J. Doyle, *Strain*, 2016, **52**, 380–399.
8 T. H. Petersen, E. A. Calle, M. B. Colehour and L. E. Niklason, *Cells Tissues Organs*, 2012, **195**, 222–231.
9 E. Claes, J. M. Atienza, G. V. Guinea, F. J. Rojo, J. M. Bernal, J. M. Revuelta and M. Elices, *Conf. Proc. IEEE Eng. Med. Biol. Soc.*, 2010, **2010**, 3792–3795.
10 A. V. Kamenskiy, Y. A. Dzenis, S. A. J. Kazmi, M. A. Pemberton, I. I. Pipinos, N. Y. Phillips, K. Herber, T. Woodford, R. E. Bowen, C. S. Lomneth and J. N. MacTaggart, *Biomech. Model. Mechanobiol.*, 2014, **13**, 1341–1359.
11 J. T. Keyes, D. G. Haskett, U. Utzinger, M. Azhar and J. P. Vande Geest, *J. Biomech. Eng.*, 2011, **133**, 075001.
12 M. Stoiber, B. Messner, C. Grasl, V. Gschlad, H. Bergmeister, D. Bernhard and H. Schima, *Exp. Mech.*, 2015, **55**, 1591–1595.
13 C. Grasl, H. Bergmeister, M. Stoiber, H. Schima and G. Weigel, *J. Biomed. Mater. Res., Part A*, 2010, **93**, 716–723.
14 T. Shazly, A. Rachev, S. Lessner, W. S. Argraves, J. Ferdous, B. Zhou, A. M. Moreira and M. Sutton, *Exp. Mech.*, 2015, **55**, 41–51.
15 J. J. Stankus, L. Soletti, K. Fujimoto, Y. Hong, D. A. Vorp and W. R. Wagner, *Biomaterials*, 2007, **28**, 2738–2746.
16 E. E. van Haaften, C. V. C. Bouten and N. A. Kurniawan, *Cells*, 2017, **6**, 19.
17 G. A. Holzapfel, *J. Theor. Biol.*, 2006, **238**, 290–302.
18 G. S. Kassab, *J. R. Soc., Interface*, 2006, **3**, 719–740.
19 F. Safshekan, M. Tafazzoli-Shadpour, M. Abdouss and M. B. Shadmehr, *Materials*, 2016, **9**, 456.
20 V. Bonito, A. I. Smits, O. J. Goor, B. D. Ippel, A. Driessen-Mol, T. J. Münker, A. W. Bosman, T. Mes, P. Y. Dankers and C. V. Bouten, *Acta Biomater.*, 2018, **71**, 247–260.
21 V. Bonito, PhD thesis, Eindhoven University of Technology, 2018.
22 L. Soffer, X. Wang, X. Zhang, J. Kluge, L. Dorfmann, D. L. Kaplan and G. Leisk, *J. Biomater. Sci., Polym. Ed.*, 2008, **19**, 653–664.
23 B. C. Isenberg and R. T. Tranquillo, *Ann. Biomed. Eng.*, 2003, **31**, 937–949.
24 H. Ahn, Y. M. Ju, H. Takahashi, D. F. Williams, J. J. Yoo, S. J. Lee, T. Okano and A. Atala, *Acta Biomater.*, 2015, **16**, 14–22.
25 G. Konig, T. N. McAllister, N. Dusserre, S. A. Garrido, C. Iyican, A. Marini, A. Fiorillo, H. Avila, W. Wystrychowski, K. Zagalski, M. Maruszewski, A. Linthurst, L. Cierpka, L. M. De and N. L'Heureux, *Biomaterials*, 2009, **30**, 1542–1550.
26 R. Gauvin, M. Guillemette, T. Galbraith, J.-M. Bourget, D. Larouche, H. Marcoux, D. Aubé, C. Hayward, F. A. Auger and L. Germain, *Tissue Eng., Part A*, 2011, **17**, 2049–2059.
27 J. Johnson, D. Ohst, T. Groehl, S. Hetterscheidt and M. Jones, *J. Tissue Sci. Eng.*, 2015, **6**, 1000151.